Computers in Biology and Medicine 195 (2025) 110574

Contents lists available at ScienceDirect

Computers in Biology and Medicine

journal homepage: www.elsevier.com/locate/compbiomed

An in silico study reveals how architectural and mechanical cues jointly regulate angiogenesis and bone regeneration in 3D printed scaffolds

Chiara Dazzi [a,b], Kian F. Eichholz [c], Fiona E. Freeman [c,d,e,f,g,h,i], Daniel J. Kelly [c,g,j,k], Sara Checa [a,l,*]

[a] *Julius Wolff Institute, Berlin Institute of Health, Charité – Universitätsmedizin Berlin, Berlin, Germany*
[b] *Berlin-Brandenburg School for Regenerative Therapies, Berlin, Germany*
[c] *Trinity Centre for Biomedical Engineering, Trinity Biomedical Sciences Institute, Trinity College Dublin, Dublin, Ireland*
[d] *School of Mechanical and Materials Engineering, Engineering and Materials Science Centre, University College Dublin, Dublin, Ireland*
[e] *Centre for Biomedical Engineering, University College Dublin, Belfield, Dublin, Ireland*
[f] *Conway Institute of Biomolecular and Biomedical Research, University College Dublin, Dublin, Ireland*
[g] *Department of Mechanical Manufacturing, and Biomedical Engineering, School of Engineering, Trinity College Dublin, Dublin, Ireland*
[h] *CÚRAM Research Ireland Centre for Medical Devices University of Galway, Galway, Ireland*
[i] *I-Form Centre, School of Mechanical and Materials Engineering, University College Dublin (UCD), Dublin, Ireland*
[j] *Department of Anatomy and Regenerative Medicine, Royal College of Surgeons in Ireland, Dublin, Ireland*
[k] *Advanced Materials and Bioengineering Research Centre (AMBER), Royal College of Surgeons in Ireland and Trinity College Dublin, Dublin, Ireland*
[l] *Institute of Biomechanics, Hamburg University of Technology, Hamburg, Germany*

ARTICLE INFO

Keywords:
Bone scaffolds
Computer models
Bone regeneration
Large bone defects
Angiogenesis
3D printing
Mechanobiology

ABSTRACT

The treatment of large bone defects is an unmet clinical need. 3D printed scaffolds offer a promising solution, however they are still not widely employed in clinical practice due to inconsistent healing outcomes and limited understanding of the underlying regeneration mechanisms. To address this, we developed a computer model for 3D printed scaffold-guided bone regeneration and angiogenesis. Our novel computer model successfully recapitulated the bone regeneration process within two 3D printed scaffold architectures: one comprised of microfibres of 20 μm diameter fabricated by melt electrowriting and another comprised of larger diameter fibres of 200 μm fabricated by fused deposition modelling. Thereafter, the model was employed to further assess the specific contribution of structural and mechanical cues on vascularisation and bone formation. We found that scaffolds fabricated by melt electrowriting enhanced bone formation because of the advantageous architectural features such as high surface-area-to-volume ratio, despite the lower mechanical stiffness. Additionally, their high open porosity facilitated vessel infiltration and induced mechanical strains accelerating vessel growth as compared to fused deposition modelling scaffolds. However, the small pore size on the outer surface might limit the invasion of larger vessels, which is expected to occur at the later stages of healing. Understanding how scaffold architecture and mechanical properties jointly orchestrate angiogenesis and bone formation is essential for optimising scaffold design and enhancing the regeneration of large bone defects. *In silico* models like the one presented in this study hold great promise for advancing scaffold design and enhancing clinical outcomes.

1. Introduction

Bone tissue has the ability to regenerate without the formation of scar tissue. However, bone defects exceeding a critical size do not heal spontaneously and their treatment remains a clinical challenge. Current treatment strategies (e.g., autologous bone grafting, Masquelet technique, and the use of growth factors) have several drawbacks, including the need for a second surgery, limited graft availability, and donor site morbidity, among others [1,2]. In the last decades, research in this field has focused on 3D printed scaffolds as a treatment alternative, capable of providing mechanical support to the healing site while guiding and promoting endogenous bone regeneration. Although several preclinical and clinical studies have shown encouraging results in terms of bone regeneration [3–10], revascularisation of large scaffolds is one of the

---

* Corresponding author.

E-mail addresses: chiara.dazzi@bih-charite.de (C. Dazzi), eichholk@tcd.ie (K.F. Eichholz), fiona.freeman@ucd.ie (F.E. Freeman), KELLYD9@tcd.ie (D.J. Kelly), sara.checa@tuhh.de (S. Checa).

https://doi.org/10.1016/j.compbiomed.2025.110574
Received 20 March 2025; Received in revised form 22 May 2025; Accepted 10 June 2025

major hurdles to their clinical adoption.

The architecture of bone scaffolds can largely influence the level of vascularisation and bone regeneration [11,12]. Geometrical properties of the scaffolds, such as pore size, porosity, surface area and surface-area-to-volume ratio, were found to affect the cellular and angiogenic processes through the scaffold pores and therefore the bone healing progression in experimental studies [7,13–22]. Pores larger than 300 μm are known to promote cell migration [14]. High porosities, in the range 70–80 %, proved to enhance osteogenic proliferation and differentiation compared to 60 % porosity [23]. Although pores larger than 300 μm promoted cell proliferation [14], no significant correlation was found between cell proliferation and pore size in other experimental works [15,18]. Medium-sized pores (470–590 μm) were found to promote vascularisation as compared to cases where pores were either bigger (>590 μm) [15] or smaller (<400 μm) [19]. However, smaller pores and thus a higher available surface area were shown to be beneficial for cell attachment [20]. A high surface-area-to-volume ratio allows optimal cell attachment [21,22] and appears to be more beneficial for bone regeneration [7]. Due to the complexity of these interactions and contradicting results reported in these studies, it is difficult to derive conclusions on how to tune scaffold parameters to promote bone and vessel formation.

Beyond the direct interaction between cells and the scaffold geometrical features, the specific scaffold architecture affects its mechanical properties and thus the share of load transferred to cells and tissues within the healing region. Mechanical signals, such as stresses and strains, are known to influence bone and vessel formation patterns. *In vitro* studies have found that vessels align along the principal strain direction at moderate strain levels (<10 %) [24], while at high strain levels (>10 %), they re-orient orthogonal to it [25–28]. Strains also modulate endothelial cell (EC) proliferation and thus vessel elongation: low strains inhibit apoptosis and increase ECs proliferation, while large strains have the opposite effect [29–32]. Mechanical strains within the healing zone play a major role in the bone regeneration process as well: moderate interfragmentary strains promote bone formation, while excessively high or low strains impair healing and can lead to delayed healing or non-union [33]. In this context, scaffold design plays a crucial role in modulating these mechanical signals within the healing region. However, there is a lack of understanding of how different scaffold designs impact the local mechanical environment surrounding the cells and affect vessel and bone formation during scaffold-aided bone regeneration.

3D printing techniques allow the production of scaffolds with tailored and highly controlled architectural features. For example, fused deposition modelling (FDM) allows the fabrication of scaffolds with large interconnected pores, while melt electrowriting (MEW) allows the 3D printing of micron and sub-micron fibres, facilitating scaffold designs with higher porosity and higher surface-area-to-volume ratios. Scaffolds fabricated by FDM and MEW have previously been shown to promote large bone defect regeneration and revascularisation in *in vivo* studies [8–10]. In particular, Eichholz and colleagues [34] showed that PCL scaffolds fabricated by MEW and FDM enhanced bone regeneration and angiogenesis in a rat segmental defect, as compared to the control empty case. The amount and pattern of the newly regenerated bone differed within the MEW and FDM scaffolds, with increased bone formation observed within the MEW group. Interestingly, FDM scaffolds were found to promote higher vessel ingrowth. However, how the scaffold micro-architecture influences the local mechanical environment within the callus, the cellular processes within the pores, and thus vessel and bone formation patterns, is not fully understood and difficult to assess through experimental approaches alone.

Computer models enable the systematic investigation of how scaffold architectural cues influence the induced mechanical environment, as well as bone regeneration and angiogenesis processes. Several computer models have helped to identify the scaffold features promoting bone regeneration [35–37] and angiogenesis [38–41]. Sun et al. [38] demonstrated that scaffold porosity played a more dominant role in affecting bone formation and angiogenesis compared with pore size. However, their model was not directly compared to *in vivo* studies. Perier Metz et al. [42] found that a lower scaffold surface-area-to-volume ratio is beneficial for bone regeneration due to enhanced cellular migration, however, they did not consider angiogenesis in the model. Nasello et al. [43] showed that the osteogenic response depends on the mechanical environment induced by the scaffold, however, they did not investigate the influence of the scaffold architecture on the regeneration process and did not account for angiogenesis. A comprehensive investigation of the relative role of mechanics and scaffold architectures on bone and vessel formation processes in large bone defects is still missing.

This study aimed to investigate how the scaffold geometrical features resulting from different 3D printing techniques (MEW and FDM) and the induced mechanical environments affect bone regeneration and angiogenesis within large bone defects. To achieve this, a computer model of scaffold-guided bone regeneration including angiogenesis was built to replicate a previously published experimental setup [34]. The computer model was first compared to the experimental results and then used to gain new insights into the role of the scaffold architecture and the mechanical environment on angiogenesis and bone regeneration in large bone defects.

2. Materials and methods

2.1. *Experimental setup*

The *in silico* model for bone regeneration was based on a previously published experimental study by Eichholz and colleagues [34]. Briefly, 4.8 mm bone defects were realised in the mid-diaphyseal femur of 12-week-old male Wistar Han rats ($n = 9$ per scaffold type) stabilised with a PEEK internal fixation plate and augmented with 3D printed polycaprolactone (PCL) scaffolds. Two distinct scaffold designs were fabricated by two 3D printing techniques: Fused deposition modelling (FDM) and Melt electrowriting (MEW). MEW scaffolds were produced using a custom-built MEW printer [44] as previously described [34], with a height of 4.8 mm, a diameter of 4 mm, and a fibre diameter of 20 μm. FDM scaffolds were printed using a commercially available 3D printer as previously described [45,46] (3DDiscovery, RegenHU), with a height of 4.8 mm, a diameter of 4 mm, and a fibre diameter of 200 μm. Scaffolds were designed to obtain comparable total surface areas. Primarily due to inherent differences in the technologies, FDM scaffolds resulted in lower porosity (76.1 % vs. 97.6 %) and lower surface area-to-volume ratio (18.04 mm^2/mm^3 vs. 201.31 mm^2/mm^3) compared to MEW scaffolds. FDM scaffolds were also printed with a larger pore size (1.2 mm vs. 0.6 mm). All scaffolds were coated in calcium phosphate comprised of a nano-needle shaped structure using a wet precipitation method as previously described [47], with needle shaped mineral aggregates being approximately 100 nm in length and 37 nm in diameter, and resulting in similar total mineral quantities (297 ± 130 μM for FDM, 340 ± 55 μM for MEW) due to the comparable surface areas. Scanning electron microscopy (SEM) was used to visualise the architectures of the printed scaffolds and the coating (Supplementary Material, Fig. S1). The healing progression was assessed by *in vivo* μCT at 6 and 12 weeks post-surgery. At 12 weeks post-surgery, animals were sacrificed and histological analyses were conducted to investigate tissue deposition and vessel ingrowth. This animal procedure and study was approved by the ethics committee in Trinity College Dublin and the Health Products Regulatory Authority (HPRA) in Ireland (Approval—AE19136/P087).

2.2. *In silico multi-scale model coupling mechanics and biology*

To investigate how the MEW and FDM scaffold architectures and the induced mechanical environments affect bone and vessel formation within large bone defects, a multiscale computational framework for scaffold-guided bone regeneration and vessel growth was developed. A computer model for scaffold-guided bone regeneration [42] was adapted to replicate the previously published *in vivo* experiment detailed in the paragraph above [34] and consisting of a large rat femoral osteotomy stabilised with an internal fixator and augmented with PCL scaffolds fabricated by FDM or MEW. The computer model was expanded to include a description of the mechano-regulation of angiogenesis and its crosstalk with chondrogenesis and osteogenesis. The model couples Finite Element Models (FEMs) at the tissue level, to determine the mechanical environment within the scaffold, to Agent-Based models (ABMs) at the cell level, describing the biological processes occurring throughout the healing process. The mechanical environment influences cell processes such as cell proliferation, migration, differentiation and apoptosis while the newly deposited tissue, predicted by the ABMs, informs the FEMs in terms of updated tissue properties (Fig. 1). A detailed description of the two modules is provided in the following sections.

2.3. Quantification of the mechanical environment

The FEM of the rat femoral osteotomy was developed in the commercial software Abaqus (Abaqus 3DEXPERIENCE R2019x) to assess the mechanical environment within scaffolds. The computer model included the cortical bone, the marrow cavity, the internal fixation plate screwed to the bone and the FDM or MEW scaffolds within the defect and surrounded by a callus. Based on µCT images, the cortical bone was modelled as a hollow cylinder with a cortical thickness of 1 mm surrounding the marrow cavity. The bone defect was mimicked by opening a 4.8-mm-wide gap in the middle of the bone. The internal fixation plate and screws were generated according to the technical drawings with the screw body approximated as a cylinder. The callus was defined based on previous studies [37,49] relying on histological data [50]. Scaffolds were modelled using Abaqus (Abaqus 3DEXPERIENCE R2019x) according to the CAD designs in Eichholz et al., 2022 [34]. The callus, cortical bone and bone marrow were assumed to behave as poroelastic materials while the materials of the internal fixation plate (PEEK), screws (stainless steel) and scaffolds (PCL with nnHA coating) were modelled as linear elastic (Table I). FDM scaffolds were meshed using 3D quadratic tetrahedral elements (Abaqus element type C3D10MP) of average size 0.2 mm, while MEW struts were meshed using quadratic beam elements (B32) with a diameter of 0.02 mm and a characteristic length of 0.2 mm. All the measurements of the FEM are reported in the Supplementary Material (Fig. S2). For the FDM, the callus and scaffold meshes were merged to create a unique part with common nodes to avoid computationally expensive constraint definition between the two parts. Since beam and 3D elements have different degrees of freedom, a merging operation was not possible for the MEW scaffold. The beam-based scaffold elements were constrained to be embedded within the 3D callus elements.

Loading conditions aimed to simulate the peak load experienced during normal walking. An axial compressive load of 25 N (equivalent to 6 body weight (BW)) was applied at the proximal bone end [51]. Additionally, two tangential forces of 3 N were applied to the proximal bone surface in the anteroposterior and medial-lateral directions, creating bending loads (resulting in a 10.7 BW mm moment at the femoral mid-shaft) [51]. The distal bone surface was fully constrained. A pore pressure boundary condition was set to zero on the external surface of the callus domain.

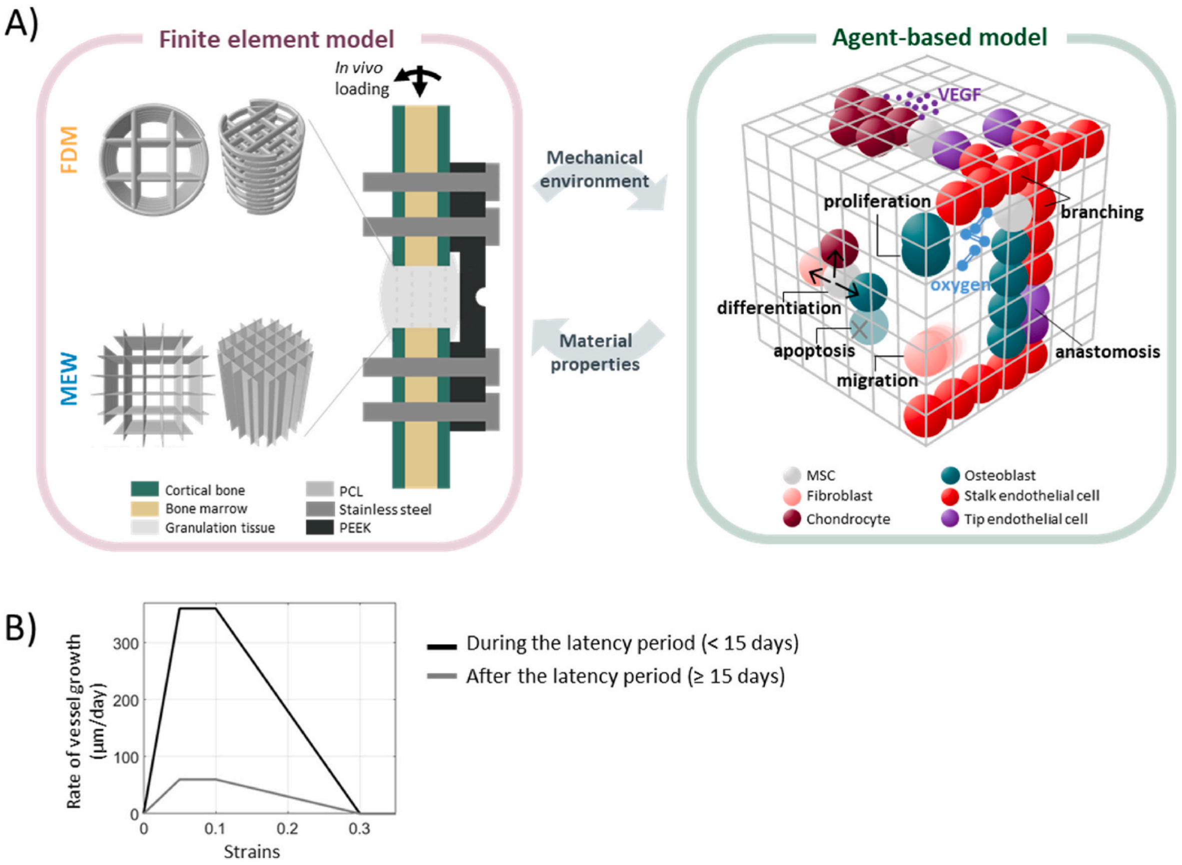

Fig. 1. A coupled finite element/agent-based model. A) Schematic representation of the bi-directional interaction between the FEM and the ABM. B) Mechanics-dependent rate of vessel growth implemented in the model, based on experimental observation [29–32,48].

Table 1
Tissue and fixation system material properties.

Material	Young's modulus (MPa)	Poisson's ratio	Permeability (10^{-14} s m^4/N)	Bulk modulus grain (MPa)	Bulk modulus fluid (MPa)
Fixation plate (PEEK)	3800	0.3	–	–	–
Screws (stainless steel)	210000	0.3	–	–	–
Scaffolds (PCL)	350[b]	0.33	–	–	–
Granulation tissue	0.2[a]	0.167[a]	1[a]	2300[a]	2300[a]
Fibrous tissue	2[a]	0.167[a]	1[a]	2300[a]	2300[a]
Cartilage	10[a]	0.3[a]	0.5[a]	3700[a]	2300[a]
Immature bone	1000[a]	0.3[a]	10[a]	13940[a]	2300[a]
Mature bone	5000[a]	0.3[a]	37[a]	13940[a]	2300[a]
Cortical bone	5000[a]	0.3[a]	0.001[a]	13920[a]	2300[a]
Bone marrow	2[a]	0.167[a]	1[a]	2300[a]	2300[a]

[a] [52].
[b] [53–59].

2.4. Description of the biological activities

The ABM consisted of self-written codes in C++, to simulate the biological processes taking place throughout the bone healing process. The healing region was discretized into a 3D lattice (spacing 20 μm [60]) where each point corresponded to an available position for cells. The following cell phenotypes were included in the model: mesenchymal stromal cells (MSC), fibroblasts, chondrocytes, immature osteoblasts, mature osteoblasts and ECs. To simulate the MSCs and vessel invasion from the bone marrow cavity and periosteum, initially 30 % [52] and 2 % [61] of available positions were filled with MSCs and ECs, respectively. Cellular processes included in the model are MSCs differentiation, MSCs and fibroblasts migration, cell proliferation, cell apoptosis and vessel growth. All activity rates are based on the available literature (Table II). MSC differentiation into other cell phenotypes, cell proliferation and apoptosis are regulated by a mechanical stimulus combining octahedral shear strain and fluid flow [52]. Low levels of mechanical stimulus promote bone formation, moderate levels support cartilage development, and high levels lead to fibrous tissue formation. To incorporate the surface-guided migration and tissue deposition observed experimentally [62–64], cell migration, differentiation and subsequent new tissue formation were allowed to occur only on top of existing surfaces (scaffold or previously deposited tissues). To simulate the reduced biological activity observed experimentally in large bone defects [2], a latency period of 15 days was implemented, after which cell activity rates were reduced [42,64] (Table 2).

A description of angiogenesis and its interaction with the bone regeneration process was added to the ABM. Vessels were modelled as a sequence of ECs occupying subsequent lattice points. Three main events characterised the development of the vascular network: (1) sprout growth, (2) the formation of a new sprout from an existing one (branching), (3) the fusion of the sprout tip to another sprout (anastomosis) [65]. Sprout growth is led by the migration of the tip ECs, followed by proliferating stalk ECs. We modelled sprout growth as influenced by either mechanical or chemical cues, including a stochastic component to account for the biological factors not included in the model. The leading tip ECs of each sprout probed the local environment and determined the direction of vessel growth based on three options with assigned probabilities: (1) following a rule based on principal strain direction and magnitude (p_mech = 20 %) [65], (2) towards high concentrations of hypertrophic chondrocytes (p_chem = 40 %), (3) towards a random direction (p_stoch = 40 %). Probability values were identified through a parameter sweep analysis in a previous coupled *in vivo/in silico* study of angiogenesis during the early stages of bone regeneration [65]. P_chem aims to replicate experimental observations whereby chondrocytes mature towards hypertrophic chondrocytes during bone regeneration and start secreting VEGF [66]. VEGF attracts ECs into the mineralised matrix, promoting vascularity and stimulating matrix metalloproteinases to degrade the cartilage matrix [67,68]. The rule based on principal strains is derived from the available literature and has already been tested against experimental data in our previous work [65]. Briefly, vessels were assumed to grow along the direction of principal strains for low strain levels (5 %) [24]. To minimise the stress experienced by the cells, vessels gradually avoid the principal strain direction and orient themselves fully perpendicular for strains above 10 % [25–28,69]. Strain magnitude was found experimentally to affect ECs proliferation rate as well [29–32,48], therefore the vessel rate of growth was modelled as dependent on the local strain level, reaching its maximum for strains between 5 % and 10 % (Fig. 1B). The vessel growth rate was assumed to be higher during the latency period in agreement with the experimental observation that vessels grow faster during the early healing phase [70]. The maximum vessel growth rate after the latency period was estimated in order to obtain a vessel density comparable to the experiment after 12 weeks. Furthermore, tip ECs were assumed to stop migrating if the principal strains were above 30 %, according to the reduced vascularity observed under cyclic compressive

Table 2
Cell activity rates during (<15 days) and after (≥15 days) the latency period, based on [42,65].

Cell type	Proliferation rate (day^{-1})		Apoptosis rate (day^{-1})	Differentiation rate (day^{-1})		Migration speed ($\mu m.h^{-1}$)	Vessel growth rate ($\mu m.day^{-1}$)[e]	
	<15 days	≥15 days		<15 days	≥15 days		<15 days	≥15 days
MSC	0.6[a]	0.3[b]	0.05[a]	0.3[a]	0.15[b]	30[c]	–	–
Fibroblast	0.55[a]	0.28[b] 5	0.05[a]	–	–	30[c]	–	–
Chondrocyte	0.2[a]	0.1[b]	0.1[a]	–	–	–	–	–
Osteoblast	0.3[a]	0.15[b]	0.16[a]	–	–	–	–	–
ECs	–	–	–	–	–	–	360[d]	60[f]
			–			–		

[a] [60].
[b] [42,64].
[c] [74].
[d] [75].
[e] Maximum growth rate when strains are between 5 % and 10 % (Fig. 1B).
[f] Estimated to obtain vessel density comparable to the experiment after 12 weeks.

strains higher than 30 % [71]. The extent and morphology of the vascular network influence other cellular processes during bone regeneration since oxygen diffusion is limited to 100–200 μm from blood vessels [72]. We have included the effect of vascularity on the cell differentiation process by assuming that MSCs in a mechanical environment favourable for bone formation, will differentiate into chondrocytes if there are no blood vessels within a 100 μm distance [73].

2.5. Simulation setup

An automatic coupling between the FEM and ABM was implemented using C++ coding. The code uses writing and reading functions to transfer information between the FEM and the ABM in an iterative manner. The whole loop is run iteratively over a total healing period of 12 weeks, with one iteration corresponding to one healing day. All simulations were performed on a server equipped with an Intel(R) Xeon (R) Gold 6248R CPU @ 3.00 GHz and 376 GB of RAM. Each simulation took approximately 5h (MEW) or 10h (FDM) for the 12 weeks of healing.

2.6. In silico output analysis

Computer model predictions for both MEW and FDM scaffolds were qualitatively and quantitatively compared to experimental data. Dedicated post-processing codes were developed to obtain images and data similar to the experiment and are detailed in the following sections. Due to the stochastic nature of the model, five simulations were run for each simulated scenario. The median simulation in terms of regenerated bone volume was chosen to produce all the 3D and 2D images.

2.6.1. Comparison of regenerated tissue predictions to experimental data

Computer model predictions for both MEW and FDM scaffolds were qualitatively compared to the experimental μCT and histological images, and quantitatively to the bone volume computed from μCT. μCT-like 3D images were obtained by converting the predicted 3D lattice into a binary image (1 = bone, 0 = not-bone), visualised then using ImageJ module VolumeViewer [76]. Bone 3D volume was quantified within the defect region, as in the experiment, by counting the number of lattice points occupied by bone and multiplying it by the point volume (8×10^{-6} mm^3). To obtain histology-like 2D images, each lattice point from the mid-longitudinal plane was assigned a colour representing the predicted tissue at that location, by using the same colour palette as in the Goldner's Trichome or Safranin O staining: dark green for bone, pink for fibrous tissue and red for cartilage tissue. Background tissues were assigned a colour similar to the experimental images.

2.6.2. Analysis of the influence of mechanics and scaffold architecture on bone regeneration

To investigate the role of the mechanical environment on bone regeneration, the mechanical stimulus distribution in the mid-longitudinal section was plotted both post-surgery and after 12 weeks, for both scaffolds. Each lattice point in the mid-longitudinal plane was assigned a colour representing the favoured tissue at that location based on the predicted mechanical stimulus [52]. The volumes characterised by a mechanical stimulus favourable for bone tissue formation were calculated as %/total regenerated volume both post-surgery and after 12 weeks. To understand the effect of scaffold architecture on bone regeneration, specific cellular activities were analysed for both scaffolds. Osteoblast proliferation and differentiation were tracked over time within the healing region by measuring the number of osteoblasts proliferating and the number of MSCs differentiating into osteoblasts, respectively. Lastly, the percentage of MSCs that could not differentiate into bone due to a lack of neighbouring surfaces was monitored within both scaffolds over time.

2.6.3. Comparison of vascularisation to experimental data

The predicted vascular network was quantitatively compared to the experimental vessel density computed within a region of interest (ROI). Specifically, simulation results were post-processed similar to the experiment: for each simulation (n = 5), three sections at different depths (from the midsection, 0.5 mm apart) were selected and a central region of interest (ROI) 2 × 2.5 mm^2 was considered (Fig. 5B). Vessels containing more than 3 ECs were counted and the number of vessels per unit area was computed. In addition, 3D reconstructions of the predicted vascular network were obtained by using a similar algorithm as for μCT-like images explained in section 2.5.1, by assigning 1 to lattice points occupied by vessels and then using ImageJ module 3D Viewer [77]. The total number of vessels predicted to grow over time within the healing region was monitored for both scaffolds.

2.6.4. Analysis of the influence of mechanics and scaffold architecture on vascularisation

To investigate the role of the mechanical environment on the predicted vessel growth, the distribution of absolute maximal principal strains post-surgery was extracted in the mid-longitudinal plane from the FE simulation. The volumetric percentages characterised by strain ranges known to influence vessel growth were computed for both MEW and FDM. In addition, the number of vessels located in strain regions detrimental to vessel growth (strains >30 %) was tracked over time within both scaffolds. To understand the influence of the scaffold architecture on vessel growth, the rate of vessel growth was set independent of the mechanical strains and the number of vessels encountering the scaffold walls, and therefore prevented from growing further, was monitored over time within the two scaffolds.

2.6.5. Data analysis and statistics

Computer model predictions were compared to the experimental results, reported as mean ± standard deviation for each scaffold type. Statistical analysis of the significant differences between experimental groups has been previously reported [34]. The same statistical tests applied to the experimental results were used to analyse the *in silico* data using R (R 4.4.3) in the Posit Cloud environment (Posit Public Cloud, https://posit.cloud). Normality of the data was assessed using the Shapiro-Wilk test, while homogeneity of variance was assessed with Levene's test. For bone quantification, a two-way ANOVA was performed with Tukey post-hoc test for pairwise comparisons. For vessel quantification, a one-way ANOVA was used with Bonferroni post-hoc test. Unpaired Welch's t-tests were used to compare *in silico* vs. *in vivo* results, due to unequal variances between the two groups, for both bone volume and vessel density. The level of significance was defined as $p \leq 0.05$.

3. Results

3.1. The in silico model recapitulated the bone healing process within MEW and FDM scaffolds

In silico results in terms of newly regenerated bone were compared qualitatively and quantitatively with *in vivo* data. The model captured the increased bone formation observed experimentally within the MEW scaffold after 12 weeks. Moreover, similarly to the experiment, the model predicted the formation of small bone spicules within the FDM scaffold pores, while more rounded bone ends were observed within the MEW scaffolds (Fig. 2A). Although the model predicted the formation of bone spicules, their size was reduced compared to the *in vivo* μCTs. The volume of the regenerated bone was predicted to increase from week 6 to week 12 within both scaffolds. The total predicted bone volume computed within both scaffolds matched quantitatively with experimental results. The model slightly underestimated the bone volume within the FDM scaffold after 6 weeks, but the value was within the experimental standard deviation (Fig. 2B).

To assess the organisation of the regenerating tissues within the two scaffold architectures, histological-like images were generated from *in*

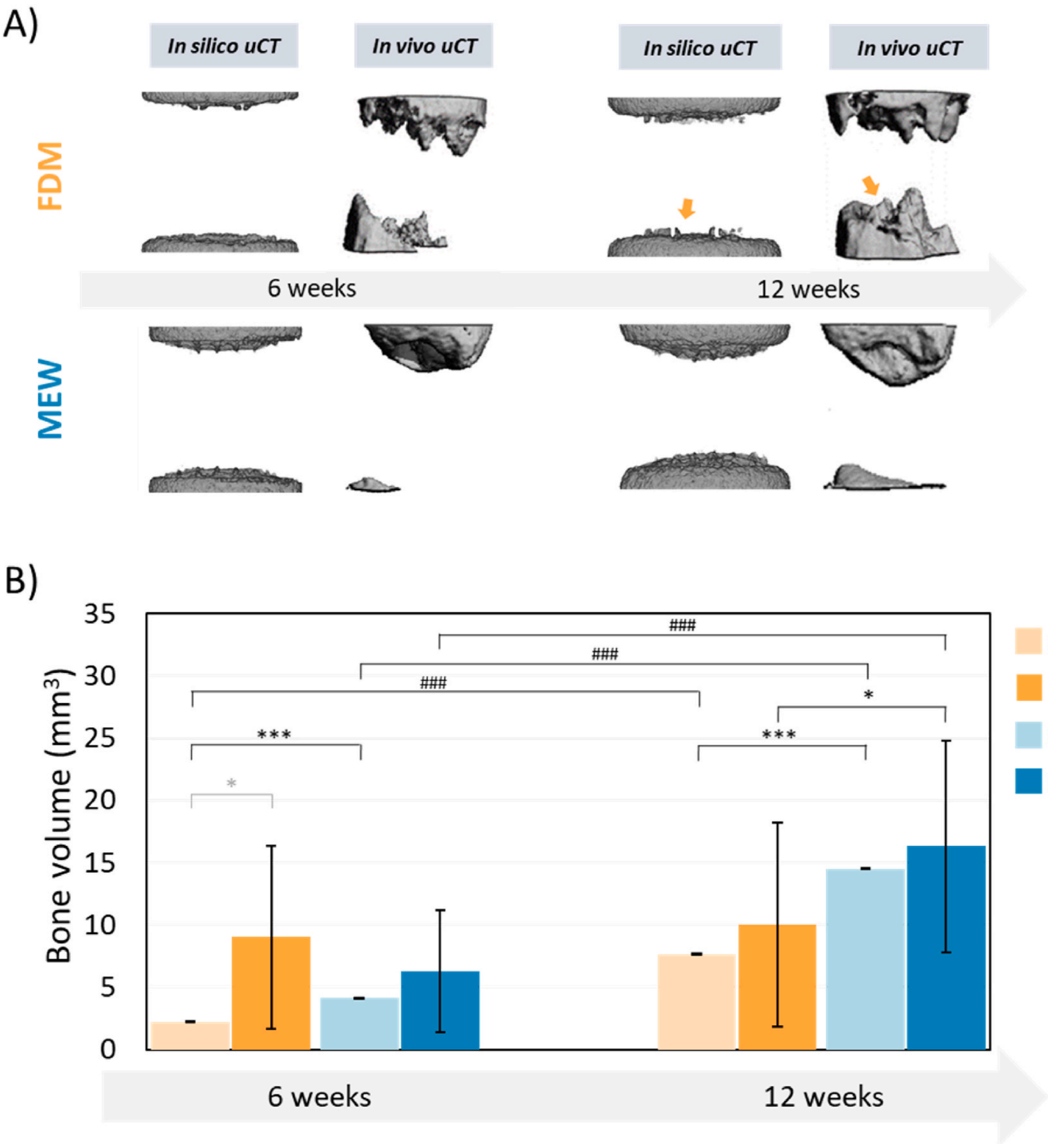

Fig. 2. Newly regenerated bone after 6 and 12 weeks. A) In silico vs. in vivo μCT reconstructions of the newly regenerated bone after 6 (left) and 12 (right) weeks within the FDM (top) and MEW (bottom) scaffolds. Orange arrows indicate the bone spicules through the FDM pores. In vivo μCTs are reproduced from Eichholz et al., 2022 [34] under Creative Commons Attribution 4.0 License. B) In silico vs. in vivo quantification of the newly regenerated bone volume after 6 and 12 weeks within the FDM and MEW scaffolds. Error bars denote standard deviation. * = statistical significance between scaffold groups using mixed-effects analysis and Tukey's multiple comparisons test (* = $p \leq 0.05$, *** = $p \leq 0.001$). # = statistical significance within scaffold groups between time-points using mixed-effects analysis and Bonferroni's multiple comparison test. (### = $p \leq 0.001$). Grey * = statistical significance between in silico and experimental groups using unpaired Welch's t-test ($p = 0.04$). (For interpretation of the references to colour in this figure legend, the reader is referred to the Web version of this article.)

silico results and compared to *ex vivo* histological images at week 12 (Fig. 3A and B). Both scaffolds were found to induce the closure of the medullary gap by bone, as reported in the Goldner's Trichome staining performed on *ex vivo* tissue sections (Fig. 3A). Fibrous and cartilaginous tissues were observed to form within both scaffolds and were quantified as a percentage over the total regenerated volume (Fig. 3C). A higher percentage of fibrous tissue was predicted within the FDM scaffold compared to the MEW (20 % vs. 12 %) (Fig. 3B and C) as a consequence of the high mechanical stimuli characterizing the regions around the scaffold walls (Fig. 4A). The growth of cartilage spots was detected within both scaffolds but denser cartilage islands were predicted to form within the FDM scaffolds compared to the MEW (12 % vs. 6 %), similar to the Safranin O staining (Fig. 3B and C). Interestingly, cartilage was observed to form in the same location both *in silico* and *in vivo*, i.e. close to the bone ends.

3.2. Advantageous architectural cues can explain the experimentally observed enhanced bone formation within MEW

The differentiation of MSCs into osteoblasts, chondrocytes or fibroblasts was modelled as dependent on the mechanical stimulus, a function of strains and fluid flow, known to be an indicator of which tissue type is more likely to form during the healing process [78]. The mechanical stimulus appears to be asymmetrically distributed due to the applied bending loads and the presence of the internal fixator on the medial (right) side, with higher (fibrous) stimulus on the lateral (left) side of both scaffolds, even though this asymmetry appears less pronounced in the FDM scaffold due to its higher stiffness (Supplementary material, File S3) and load-bearing capacity. Larger volumes favourable for bone tissue formation were found within the FDM scaffold (60 % post-surgery, 57 % after 12 weeks) as compared with the MEW scaffold (30 % post-surgery, 34 % after 12 weeks) (Fig. 4A). However, higher

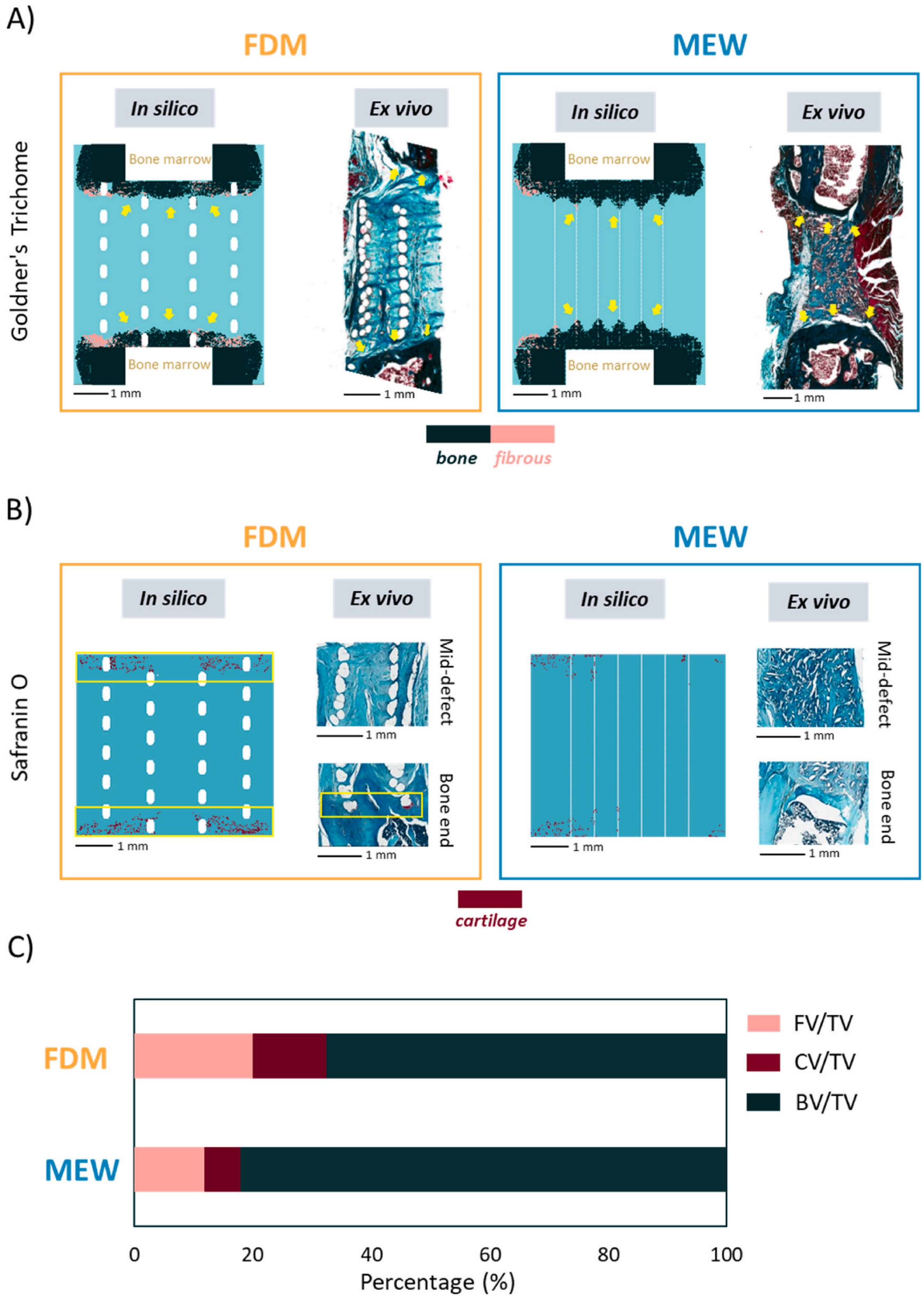

Fig. 3. Prediction of tissue organisation within scaffolds and comparison with ex vivo histological images. A) In silico vs. ex vivo Goldner's Trichome staining within the longitudinal mid-section of FDM (left) and MEW (right) scaffolds. Histological staining shows bone in dark green and unspecific soft tissue in red. Predicted fibrous tissue is shown in pink to distinguish it from cartilage, which is shown in red in B). Yellow arrows indicate bone tissue closing the bone marrow gap both in silico and ex vivo. Ex vivo images are reproduced from Eichholz et al., 2022 [34] under Creative Commons Attribution 4.0 License. B) In silico vs. ex vivo Safranin O staining within the longitudinal mid-section of FDM (left) and MEW (right) scaffolds. Histological staining shows cartilage in red. Yellow boxes highlight cartilage tissue near the bone ends, both in silico and ex vivo, within the FDM scaffold. Ex vivo images are reproduced from Eichholz et al., 2022 [34] under Creative Commons Attribution 4.0 License. C) Quantification of in silico tissue formation as a percentage of the total regenerated volume. FV= fibrous tissue volume, CV=cartilage tissue volume, BV=bone tissue volume, TV=FV + CV + BV=total regenerated tissue volume. (For interpretation of the references to colour in this figure legend, the reader is referred to the Web version of this article.)

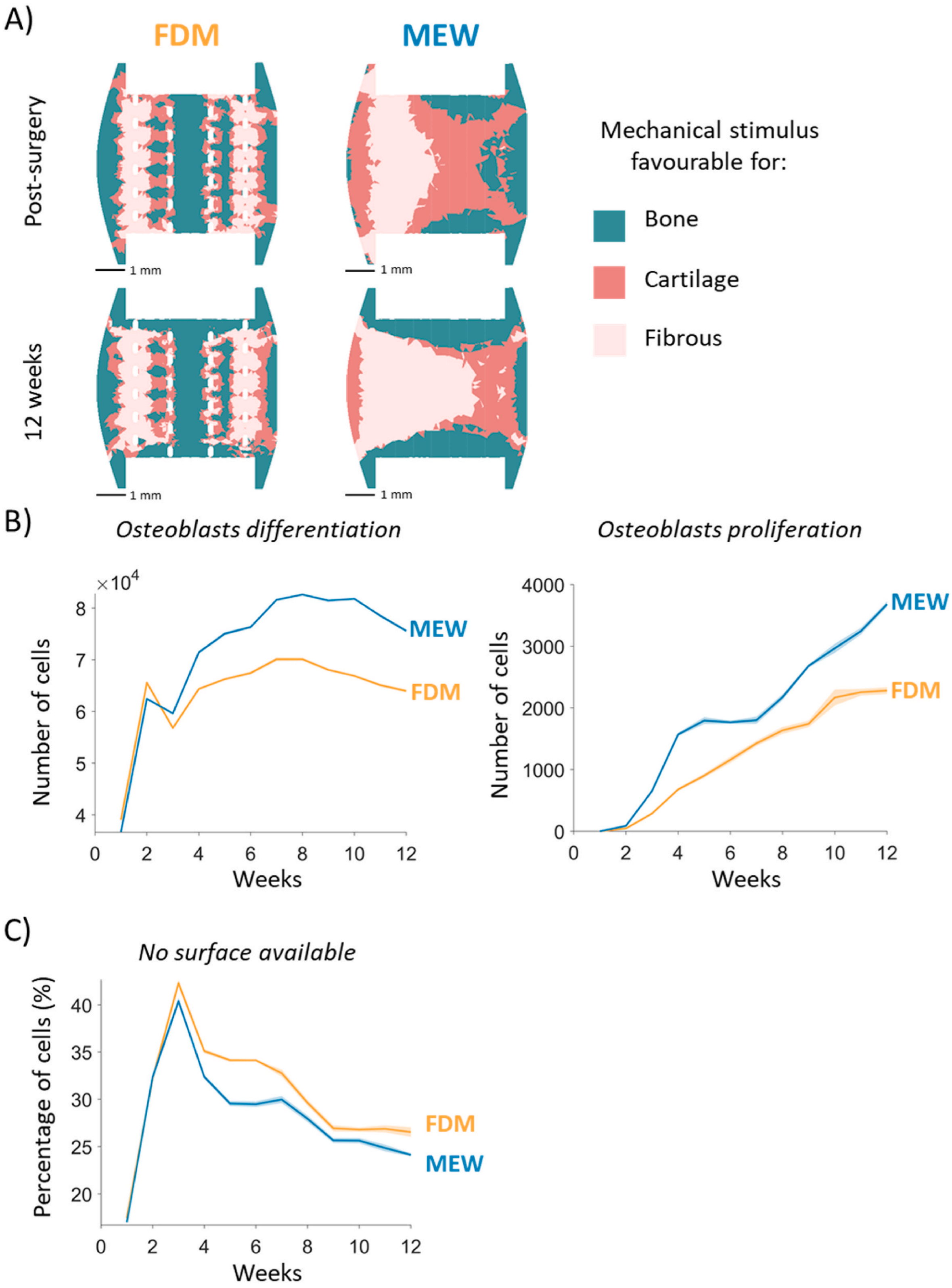

Fig. 4. The role of the mechanical environment and scaffold architecture for bone regeneration within FDM and MEW scaffolds. A) Distribution of the mechanical stimulus within the longitudinal mid-section post-surgery (top) and after 12 weeks (bottom) within the FDM (left) and MEW (right) scaffold. B) On the left, the number of cells differentiating into osteoblasts over time within FDM and MEW scaffolds; on the right, the number of proliferating osteoblasts over time within FDM and MEW scaffolds. Solid lines display the mean value, shaded areas represent the range within one standard **deviation**. C) The percentage of MSCs that could not differentiate into bone because of the lack of surfaces, over time, within FDM and MEW scaffolds. Solid lines display the mean value, shaded areas represent the range within one standard **deviation**.

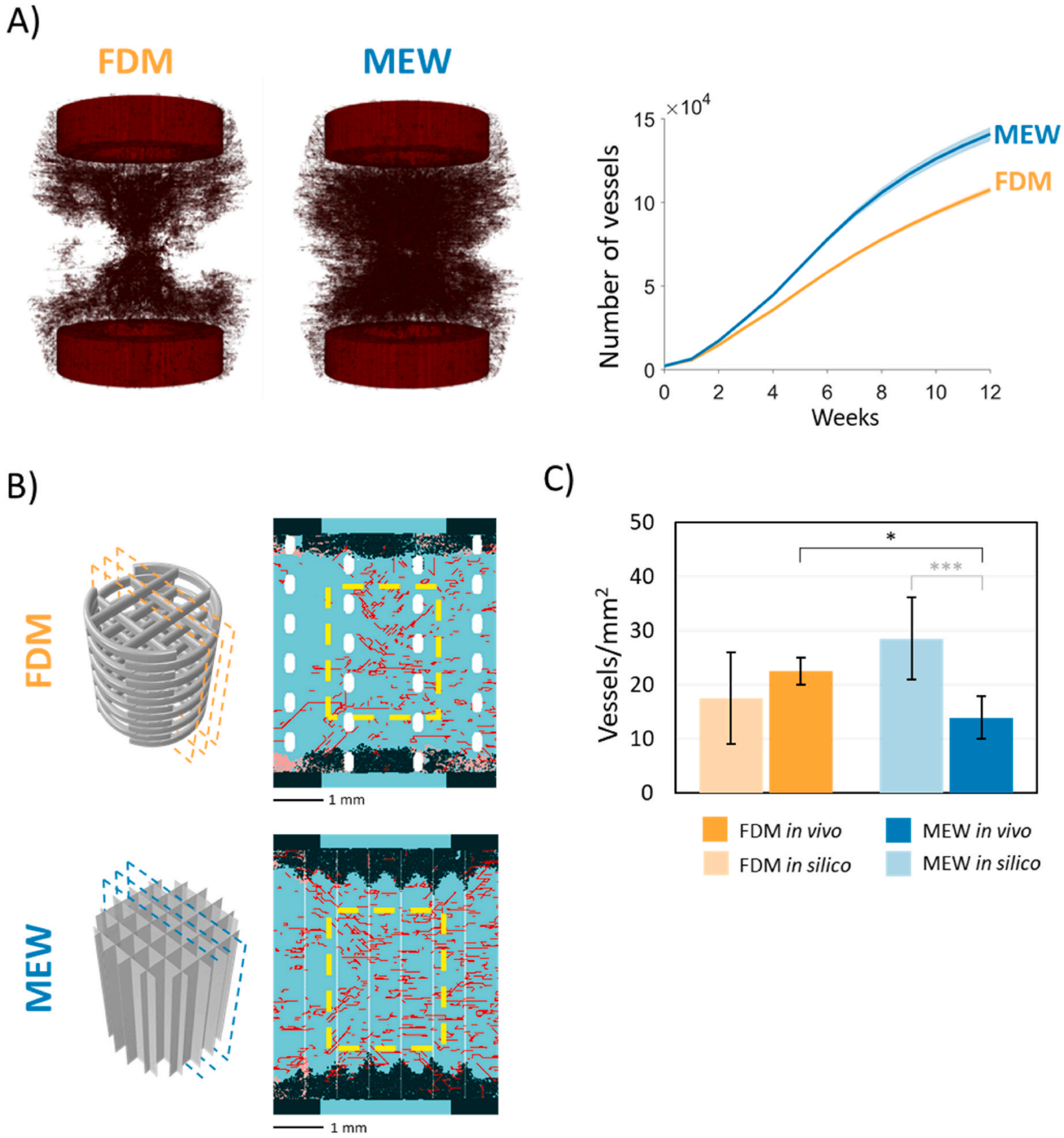

Fig. 5. Vessel ingrowth within MEW and FDM scaffolds. A) 3D reconstruction of vessels at week 12 (left) and number of vessels over time (right) within FDM and MEW scaffolds. Solid lines display the mean value, shaded areas represent the range within one standard **deviation**. B) Identification of scaffold sections (left) and the ROI (yellow square, right) selected within each section for the vessel density quantification. C) In silico vs. ex vivo quantification of vessel density within the ROI displayed in B) after 12 weeks within the FDM and MEW scaffolds. Error bars denote standard deviation. * = statistical significance between scaffold groups using unpaired t-test (* = $p \leq 0.05$). Grey * = statistical significance between in silico and experimental groups using unpaired Welch's t-test (*** = $p \leq 0.001$). (For interpretation of the references to colour in this figure legend, the reader is referred to the Web version of this article.)

proliferation and increased osteoblastic differentiation was predicted within the MEW scaffolds, in agreement with the higher level of bone formation (Fig. 4B). Within the FDM scaffolds, a high percentage of MSCs were not able to differentiate into osteoblasts due to the lack of surfaces for cell attachment and subsequent differentiation (Fig. 4C). The percentage of MSCs that could not find a surface increased sharply during the first 18 days within both scaffolds. Afterwards, the FDM curve was steadily above the MEW one (Fig. 4C).

3.3. MEW scaffolds appear to induce a more favourable mechanical environment and a more permissive scaffold architecture for vessel growth

Vessels were predicted to invade both the FDM and MEW scaffolds reaching the scaffold cores, as observed experimentally, with a more homogeneous distribution of vessels within the MEW scaffold (Fig. 5A). The total number of vessels was observed to increase over time within both scaffolds, but being higher within the MEW scaffold at every time point (Fig. 5A). After 12 weeks, in contrast to the experimental data, the predicted vessel density was higher in MEW compared to the FDM scaffold (Fig. 5C).

The mechanical strains were quantified within the callus volume and appeared generally lower within the FDM scaffold as a consequence of its higher compression stiffness (18 MPa for FDM, 0.03 MPa for MEW). The simulated compression tests for both scaffolds can be found in the supplementary material (File S3). A higher volumetric percentage characterized by strains within 5 % and 10 %, known to promote vessel growth [48], was found within the MEW scaffold (Fig. 6A). Moreover, the number of vessels encountering high strain regions (>30 %) was observed to increase over time within the FDM scaffold, while being steadily around zero within the MEW scaffold (Fig. 6B). These high strain regions were found mainly close to the FDM scaffold walls (Fig. 6A).

To assess the impact of the scaffold structure alone, the rate of vessel growth was set constant and equal to the maximum growth rate (when strains are between 5 % and 10 %). As expected, the total vessel elongation increased for both FDM and MEW scaffolds upon ruling out the effect of mechanical signals. Specifically, FDM scaffolds showed a more pronounced increase in terms of vessel elongation over time, confirming that the mechanical environment was compromising vessel ingrowth (Fig. 6C). The initial spike in the curves representing the total elongation is a consequence of the increased rate of vessel growth assumed during the latency period. Still, the total vessel elongation was predicted to be

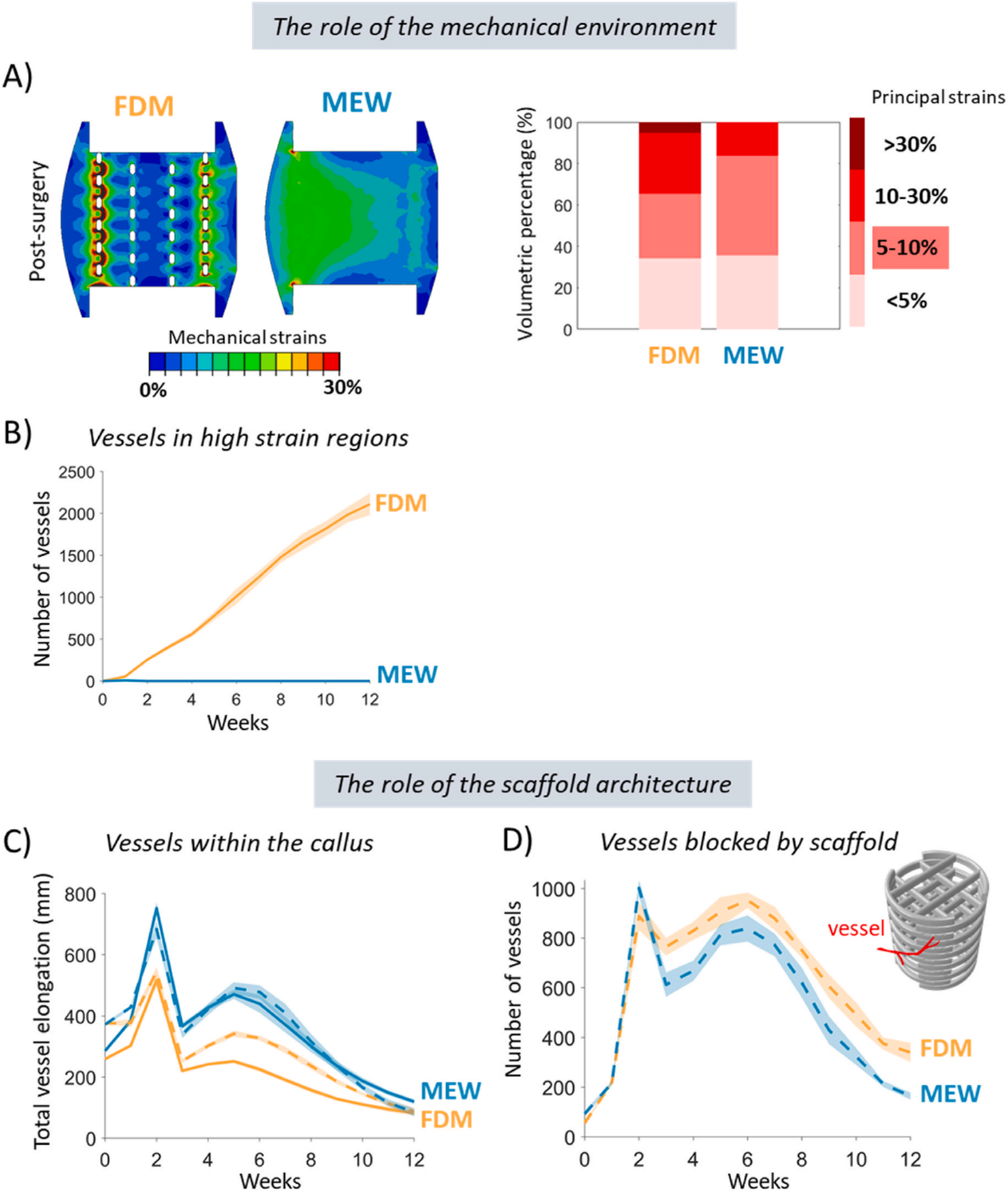

Fig. 6. The role of the mechanical environment and scaffold architecture on vessel growth within FDM and MEW scaffolds. A) Contour plot of the mechanical strains (left) and volumetric percentages characterised by relevant strain levels (right) within both scaffolds. B) Number of vessels in regions characterised by strains above 30 % within FDM and MEW scaffolds over time. Solid lines display the mean value, shaded areas represent the range within one standard **deviation**. C) Total vessel elongation when assuming a mechanics-dependent (solid lines) vs. constant (dashed lines) growth rate within FDM and MEW scaffolds over time. Shaded areas represent the range within one standard **deviation.** D) Number of vessels over time blocked by the scaffold structure within FDM and MEW scaffolds, when assuming a constant vessel growth rate. Dashed lines display the mean value, shaded areas represent the range within one standard **deviation**.

higher for the MEW scaffold as compared to the FDM scaffold, and this appeared to be linked to the more permissive scaffold architecture of MEW. Indeed, the number of vessels prevented from growing further because they were encountering the scaffold walls was computed for both scaffolds over time and found to be higher within the FDM scaffold (Fig. 6D).

4. Discussion

Three-dimensional (3D) printed scaffolds represent promising approaches to treat large bone defects, although the re-establishment of a functional vascular network is a main challenge to their translation into clinical practice. To design scaffolds capable of promoting angiogenesis and thus bone regeneration, it is necessary to gain a deeper understanding of the mechano-biological processes behind scaffold-aided angiogenesis and bone regeneration. Here we present a computer model that allows us to investigate the role of scaffold architecture and mechanical cues on angiogenesis and bone regeneration within two 3D-printed scaffolds fabricated by either FDM or MEW. Although the experimental data were previously published [34], the novelty of this study lies in the development and use of a mechano-biological computer model to separately analyse the effects of scaffold architectural cues and the induced mechanical environment on angiogenesis and bone regeneration, challenging to investigate experimentally. We show that the interplay between the mechanical environment within the scaffold and its architectural features can explain experimentally observed angiogenic and bone regeneration processes. We identified strut spacing, pore size and scaffold surface-area-to-volume ratio as important regulators of both processes.

Upon comparison of *in silico* results with experimental data [34], we found that the computer model could recapitulate key aspects of the bone healing process within MEW and FDM scaffolds, predicting the increased bone formation observed *in vivo* within the MEW scaffolds. Besides the quantification of the regenerated bone volume, the predicted bone formation patterns compared well with those observed experimentally, with rounded bone ends within the MEW scaffolds and small bone spicules through the FDM scaffold pores. Our computer model predicted other phenomena taking place during the bone regeneration process, such as the closure of the medullary gap by bone and the formation of denser cartilage islands within the FDM scaffolds. The latter can be explained by the high mechanical stimuli close to the FDM scaffold walls and indicates that there is still potential for further bone formation after 12 weeks through an endochondral ossification process, as observed experimentally [34]. It should be noted that when comparing *in silico* vs. *ex vivo* histological images, *in silico* images show large gaps between scaffold struts, whereas *ex vivo* images show stacked (FDM) or disorganised (MEW) struts. This discrepancy arises because the *in silico* scaffold structure replicates the CAD idealised geometry, while the actual 3D printed scaffold may differ as fibres tend to fuse slightly between layers. Additionally, scaffolds may deform over 12 weeks *in vivo*, particularly the soft MEW, and histological processing, including sectioning and PCL dissolution, can lead to further distortions.

Our simulations showed an asymmetrical distribution of mechanical stimuli within the scaffolds due to the applied bending loads and the presence of the internal fixator. Interestingly, bone regeneration patterns appeared only mildly asymmetrical, indicating that the mechanical stimulus is not the only factor influencing bone formation patterns. To investigate the mechano-biological processes behind the increased bone formation within the MEW scaffold, specific cellular activities were tracked throughout the bone healing simulation. As expected, increased osteoblast proliferation and differentiation were observed over time within the MEW scaffolds, despite larger volumes characterised by a mechanical environment favourable for bone tissue formation being predicted within the FDM scaffold. This suggested that the enhanced bone formation within the MEW scaffold could not be explained by the mechanical environment alone. Enhanced cell proliferation within MEW as compared to FDM scaffolds has already been observed during preliminary *in vitro* experiments by Eichholz and colleagues [34] and was associated with the higher porosity of the MEW scaffold, allowing a greater volume within which cells can proliferate. To better understand whether scaffold architectural cues were also contributing to the predicted increased osteoblast differentiation within the MEW scaffold, the percentage of MSCs that could not differentiate into the osteoblast lineage, despite being under the right mechanical stimulus, was quantified. MSCs exhibited a lower differentiation within the FDM scaffold due to the difficulty in finding available surfaces for cell attachment. This may be due to the increased distance between scaffold inner surfaces (higher pore size and lower surface-area-to-volume ratio) and agrees with other experimental studies that reported faster cell growth for shorter distances between scaffold inner surfaces [79].

Vessels were predicted to infiltrate both MEW and FDM, reaching the scaffold core, in agreement with experimental findings [34]. Notably, although the two scaffolds were predicted to be well vascularized after 12 weeks, complete bone healing was not achieved both experimentally and *in silico*. This result appears in contrast to the traditional positive correlation between vascularisation and bone regeneration. However, some studies have suggested that a more complex relationship exists between the two [80,81]. Specifically, vascularisation is essential but alone it does not guarantee bone regeneration without an appropriate osteo-inductive environment. Research has shown that, even within a vascularized environment, both optimal structural characteristics (e.g. pore size, [81]) and chemical properties (e.g. calcium ion depletion, [80]) are required to promote effective bone regeneration. Although the predicted vessel densities within a ROI were comparable to the *in vivo* ones, the computer model showed an increased vessel density within the MEW scaffold, in contrast to the experiment. To identify the factors contributing to the different vessel ingrowth predicted within the FDM and MEW scaffolds, the role of the mechanics induced within the healing region and the scaffold architectural cues were analysed independently. Larger regions characterised by levels of mechanical strains in the range 5–10 %, known to favour ECs proliferation and vessel elongation [29–32,48], were found within the callus of the MEW group. Furthermore, even though mechanical strains were generally higher within the MEW scaffold due to its lower effective stiffness, peak strains above 30 % were found at the FDM scaffold-tissue interface, further hindering vessel ingrowth within the FDM, in line with the experimental literature [71]. In addition to inducing a more favourable mechanical environment for vessel growth, MEW scaffolds appeared to have a more permissive scaffold architecture for vessel ingrowth. After knocking out the mechano-responsiveness of ECs by assuming a constant rate of vessel growth, more vessels were blocked by the scaffold walls and prevented from growing further within the FDM as compared to the MEW scaffold. The external surface of the MEW scaffold is more open for vessel infiltration (about a 50 % probability of finding an open space) compared to the FDM scaffold, which presents regions where material layers overlap and locally block the vessels coming from the periosteum.

Our study has several limitations that need to be mentioned. First, our computer model could not predict the increased vascularity observed experimentally within the FDM scaffold. We hypothesise that the mismatch between *in silico* and *in vivo* results in terms of vessel density is due to a current limitation of the model, this is that vessels are assumed to have a constant diameter of 20 μm. However, the vessel lumen grows over time, and the narrow space between struts on the MEW outer surface (space between struts = 20 μm) might prevent the infiltration of larger vessels coming from the periosteal site. In addition, we have predicted an increased vascular response from the periosteum as compared to the bone marrow (Supplementary Material, Fig. S4), in agreement with other *in vivo* studies [82,83]. It is worth noting that the majority of vessels (95 %) within the MEW scaffold *in vivo* exhibited diameters below 20 μm [34], confirming the limited ability of larger vessels to penetrate the structure. Motivated by these considerations, as a proof of concept, we have assumed a higher constant vessel diameter of 40 μm and analysed the model response in terms of vessel density within the same ROI. We found that the computer model could predict the increased vessel penetration within the FDM scaffold as compared to MEW (Supplementary Material, Fig. S5 A-B), even though vessel density was generally underestimated. Importantly, the predicted newly deposited bone slightly decreased as a consequence of the reduced vessel ingrowth but was still predicted to be higher within the MEW scaffold (Supplementary Material, Fig. S5 C-D). To improve model prediction capabilities, future work should include a dynamic vessel diameter model based on available experimental data. Some studies suggest that vessel diameter changes might be influenced by local VEGF concentrations [84] and fluid shear stresses sensed by endothelial cells [85]; however, the specific mechanisms regulating vessel diameter enlargement during vessel remodelling in bone healing remain poorly understood. Once more experimental data is available, the model could be expanded to include a computational fluid dynamics (CFD) module capable of mimicking vessel diameter adaptation to fluid shear stresses. Another factor that may contribute to the differences in vessel growth between MEW and FDM, not included in the current model, is the modulation of the inflammatory response by the scaffold architecture. Scaffold geometry can influence immune cell and cytokine behaviour [86–88], thereby affecting angiogenesis. However, inflammation peaks within 24 h and typically resolves by the end of the first week post-injury [89]. The presence of blood vessels in the scaffold core suggests that this pro-inflammatory phase has resolved, allowing a transition towards a pro-angiogenic environment within both scaffolds. Although extracellular matrix (ECM) fibres are important components in bone regeneration and angiogenesis as they provide structural support and guidance for ECM mineralization [35,90] and vascularisation [91], the deposition of the ECM was not directly modelled. Nevertheless, our model could replicate the shape of the newly formed bone ends within the two scaffolds, although FDM bone spicules appeared smaller compared to those observed experimentally. The formation of bone spicules through large scaffold pores has been already observed experimentally and has been explained as a non-standard mineralization process driven by highly aligned collagen fibres [35]. By including collagen fibre deposition, matrix degradation (mediated by MMPs - Matrix Metalloproteinases) and strain-induced remodelling, it may be possible to improve the fidelity of the developed computational framework and better capture the formation of long bone cones within the FDM scaffold pores. An alternate or complementary mechanism behind the formation of bone spicules could be the fluid shear stress-induced osteoblast polarization [92], influencing the directionality of matrix deposition [93]. A more sophisticated model including CFD, to compute fluid shear stresses within the healing region, could provide further insights behind the growth of bone spicules within scaffold pores. Moreover, vessel regression and remodelling were indirectly taken into account by reducing the vessel rate of growth after 2 weeks. Nevertheless, our approach allowed to obtain a vessel density after 12 weeks similar to the experiment. Blood flow, oxygenation and several signalling pathways are all thought to contribute to vessel regression and remodelling, however the specific mechanisms initiating those processes have been largely overlooked and are still unknown [94]. Once additional data is available, the model could be extended to incorporate aspects of vessel remodelling processes such as the vessel lumen enlargement over time. Another limitation of the current modelling approach is the indirect representation of VEGF-guided vessel growth, using hypertrophic chondrocyte density instead of quantitative modelling of VEGF gradients (e.g., PDE-based diffusion). While this simplification does not affect the conclusions presented in this study, future studies could focus on explicitly modelling VEGF diffusion. In this study, we focused only on two scaffold architectures (FDM and MEW) to investigate how mechanical cues and scaffold architectural features affect bone and vessel formation. These designs were selected to replicate a specific *in vivo* experiment [34] and allow model validation by comparing *in silico* and *in vivo* outputs. However, the developed computational framework is highly flexible, with mechanical and biological parameters easily adjustable to replicate various bone regeneration experimental conditions. This will enable to explore various scaffold designs in the future to further enrich our findings. Lastly, the geometry of the FDM scaffold was slightly simplified to reduce the computational cost of the simulation. The original scaffold geometry consisted of struts with a circular cross-section that required >1 millions elements to be discretized, resulting in a simulation time above 5 h for one single FEA. Being this an iterative model, 26 FEA are required to simulate 12 weeks of bone regeneration. To reduce the simulation time, adjacent overlapping struts were merged in pairs, resulting into a single strut with an oval-shaped cross-section. This allowed reducing the computational time of more than 5 times. It is important to mention that also the original scaffold geometry represents an idealization of the actual printed geometry.

In summary, we present here a computational framework capable of replicating the healing progression within scaffolds fabricated by two different 3D printing techniques: FDM and MEW. This approach allowed to investigate the impact of scaffold architectural and mechanical cues on bone regeneration and angiogenesis independently. We have found that beneficial architectural features such as strut spacing and surface-area-to-volume ratio can explain the increased bone formation observed within MEW scaffolds, despite inducing a mechanical environment less favourable for bone growth as compared to FDM scaffolds. Moreover, we show that MEW scaffolds present a more permissive scaffold architecture for vessel infiltration due to their high open porosity and induced mechanical strains, within the range of those reported to foster vessel growth. However, the small pore size on the outer surface can prevent larger periosteal vessels from invading the scaffold over time. This study shows the potential of combining *in silico* and *in vivo* approaches to gain a deeper understanding of the interplay between scaffold architecture and mechanical signals during bone regeneration and angiogenesis in large defects. Once validated against different scaffold designs, our computational framework could be employed to reduce and accelerate pre-clinical trials by testing the bone regeneration and angiogenic potential of new scaffold designs prior to *in vivo* implantation.

CRediT authorship contribution statement

Chiara Dazzi: Writing – review & editing, Writing – original draft, Visualization, Validation, Software, Methodology, Investigation, Formal analysis, Conceptualization. **Kian F. Eichholz:** Writing – review & editing, Investigation, Formal analysis, Data curation. **Fiona E. Freeman:** Writing – review & editing, Investigation, Formal analysis, Data curation. **Daniel J. Kelly:** Writing – review & editing, Supervision, Funding acquisition. **Sara Checa:** Writing – review & editing, Writing – original draft, Supervision, Funding acquisition, Conceptualization.

Data availability

Data will be made available on request.

Ethics statement

The animal procedure and study reported in this manuscript were approved by the ethics committee at Trinity College Dublin and the Health Products Regulatory Authority (HPRA) in Ireland (Approval—AE19136/P087). All procedures were performed in compliance with relevant laws and institutional guidelines to ensure the ethical treatment of animals. As this research involves the use of data from a previously published experiment, no new ethical approval was required.

Declaration of competing interest

The authors declare that they have no known competing financial interests or personal relationships that could have appeared to influence the work reported in this paper.

Acknowledgement

This study was funded by the German Research Foundation (DFG) through the Collaborative Research Centre (CRC) 1444, project ID: 427826188, by the Science Foundation Ireland (SFI) under grant number 12/RC/2278 and 17/SP/4721 and co-funded by the European Regional Development Fund and SFI under Ireland's European Structural and Investment Fund.

Appendix A. Supplementary data

Supplementary data to this article can be found online at https://doi.org/10.1016/j.compbiomed.2025.110574.

References

[1] E. Roddy, M.R. DeBaun, A. Daoud-Gray, Y.P. Yang, M.J. Gardner, Treatment of critical-sized bone defects: clinical and tissue engineering perspectives, Eur. J. Orthop. Surg. Traumatol. 28 (3) (2018) 351–362.

[2] C. Schlundt, C.H. Bucher, S. Tsitsilonis, H. Schell, G.N. Duda, K. Schmidt-Bleek, Clinical and research approaches to treat non-union fracture, Curr. Osteoporos. Rep. 16 (2) (2018) 155–168.

[3] J.A. Cobos, R.W. Lindsey, Z. Gugala, The cylindrical titanium mesh cage for treatment of a long bone segmental defect: description of a new technique and report of two cases, J. Orthop. Trauma 14 (1) (2000).

[4] J.C. Reichert, A. Cipitria, D.R. Epari, S. Saifzadeh, P. Krishnakanth, A. Berner, M. A. Woodruff, H. Schell, M. Mehta, M.A. Schuetz, G.N. Duda, D.W. Hutmacher, A tissue engineering solution for segmental defect regeneration in load-bearing long bones, Sci. Transl. Med. 4 (141) (2012), 141ra93-141ra93.

[5] F.A. Shah, O. Omar, F. Suska, A. Snis, A. Matic, L. Emanuelsson, B. Norlindh, J. Lausmaa, P. Thomsen, A. Palmquist, Long-term osseointegration of 3D printed CoCr constructs with an interconnected open-pore architecture prepared by electron beam melting, Acta Biomater. 36 (2016) 296–309.

[6] A.M. Crovace, L. Lacitignola, D.M. Forleo, F. Staffieri, E. Francioso, A. Di Meo, J. Becerra, A. Crovace, L. Santos-Ruiz, 3D biomimetic porous titanium (Ti6Al4V ELI) scaffolds for large bone critical defect reconstruction: an experimental study in sheep, Animals 10 (8) (2020) 1389.

[7] A.-M. Pobloth, S. Checa, H. Razi, A. Petersen, J.C. Weaver, K. Schmidt-Bleek, M. Windolf, A.Á. Tatai, C.P. Roth, K.-D. Schaser, G.N. Duda, P. Schwabe, Mechanobiologically optimized 3D titanium-mesh scaffolds enhance bone regeneration in critical segmental defects in sheep, Sci. Transl. Med. 10 (423) (2018) eaam8828.

[8] F.E. Freeman, D.C. Browe, J. Nulty, S. Von Euw, W.L. Grayson, D.J. Kelly, Biofabrication of multiscale bone extracellular matrix scaffolds for bone tissue engineering, Eur. Cell. Mater. 38 (2019) 168–187.

[9] K.F. Eichholz, P. Pitacco, R. Burdis, F. Chariyev-Prinz, X. Barceló, B. Tornifoglio, R. Paetzold, O. Garcia, D.J. Kelly, Integrating melt electrowriting and fused deposition modeling to fabricate hybrid scaffolds supportive of accelerated bone regeneration, Adv. Healthcare Mater. 13 (3) (2024) 2302057.

[10] N. Abbasi, R.S.B. Lee, S. Ivanovski, R.M. Love, S. Hamlet, In vivo bone regeneration assessment of offset and gradient melt electrowritten (MEW) PCL scaffolds, Biomater. Res. 24(1) 17.

[11] A.A. Zadpoor, Bone tissue regeneration: the role of scaffold geometry, Biomater. Sci. 3 (2) (2015) 231–245.

[12] S. Yin, W. Zhang, Z. Zhang, X. Jiang, Recent advances in scaffold design and material for vascularized tissue-engineered bone regeneration, Adv. Healthcare Mater. 8 (10) (2019) e1801433.

[13] A.R. Amini, D.J. Adams, C.T. Laurencin, S.P. Nukavarapu, Optimally porous and biomechanically compatible scaffolds for large-area bone regeneration, Tissue Eng. 18 (13–14) (2012) 1376–1388.

[14] C.M. Murphy, M.G. Haugh, F.J. O'Brien, The effect of mean pore size on cell attachment, proliferation and migration in collagen-glycosaminoglycan scaffolds for bone tissue engineering, Biomaterials 31 (3) (2010) 461–466.

[15] L.G. Sicchieri, G.E. Crippa, P.T. de Oliveira, M.M. Beloti, A.L. Rosa, Pore size regulates cell and tissue interactions with PLGA–caP scaffolds used for bone engineering, J. Tissue Eng. Regen. Med. 6 (2) (2012) 155–162.

[16] C. Wu, Y. Zhang, Y. Zhu, T. Friis, Y. Xiao, Structure–property relationships of silk-modified mesoporous bioglass scaffolds, Biomaterials 31 (13) (2010) 3429–3438.

[17] Y. Zhang, W. Fan, Z. Ma, C. Wu, W. Fang, G. Liu, Y. Xiao, The effects of pore architecture in silk fibroin scaffolds on the growth and differentiation of mesenchymal stem cells expressing BMP7, Acta Biomater. 6 (8) (2010) 3021–3028.

[18] C. Correia, S. Bhumiratana, L.-P. Yan, A.L. Oliveira, J.M. Gimble, D. Rockwood, D. L. Kaplan, R.A. Sousa, R.L. Reis, G. Vunjak-Novakovic, Development of silk-based scaffolds for tissue engineering of bone from human adipose-derived stem cells, Acta Biomater. 8 (7) (2012) 2483–2492.

[19] B. Feng, Z. Jinkang, W. Zhen, L. Jianxi, C. Jiang, L. Jian, M. Guolin, D. Xin, The effect of pore size on tissue ingrowth and neovascularization in porous bioceramics of controlled architecture in vivo, Biomed Mater 6 (1) (2011) 015007.

[20] N. Abbasi, A. Abdal-hay, S. Hamlet, E. Graham, S. Ivanovski, Effects of gradient and offset architectures on the mechanical and biological properties of 3-D melt electrowritten (MEW) scaffolds, ACS Biomater. Sci. Eng. 5 (7) (2019) 3448–3461.

[21] F.J. O'Brien, B.A. Harley, I.V. Yannas, L.J. Gibson, The effect of pore size on cell adhesion in collagen-GAG scaffolds, Biomaterials 26 (4) (2005) 433–441.

[22] T.D. Nguyen, O.E. Kadri, V.I. Sikavitsas, R.S. Voronov, Scaffolds with a high surface area-to-volume ratio and cultured under fast flow perfusion result in optimal O2 delivery to the cells in artificial bone tissues, Appl. Sci. 9 (11) (2019) 2381.

[23] J. Jiao, Q. Hong, D. Zhang, M. Wang, H. Tang, J. Yang, X. Qu, B. Yue, Influence of porosity on osteogenesis, bone growth and osteointegration in trabecular tantalum scaffolds fabricated by additive manufacturing, Front. Bioeng. Biotechnol. 11 (2023) 1117954.

[24] L.E. Claes, N. Meyers, The direction of tissue strain affects the neovascularization in the fracture-healing zone, Med. Hypotheses 137 (2020) 109537.

[25] J.H. Wang, P. Goldschmidt-Clermont, J. Wille, F.C. Yin, Specificity of endothelial cell reorientation in response to cyclic mechanical stretching, J. Biomech. 34 (12) (2001) 1563–1572.

[26] M. Moretti, A. Prina-Mello, A.J. Reid, V. Barron, P.J. Prendergast, Endothelial cell alignment on cyclically-stretched silicone surfaces, J. Mater. Sci. Mater. Med. 15 (10) (2004) 1159–1164.

[27] I.S. Joung, M.N. Iwamoto, Y.T. Shiu, C.T. Quam, Cyclic strain modulates tubulogenesis of endothelial cells in a 3D tissue culture model, Microvasc. Res. 71 (1) (2006) 1–11.

[28] J.R. Wilkins, D.B. Pike, C.C. Gibson, L. Li, Y.T. Shiu, The interplay of cyclic stretch and vascular endothelial growth factor in regulating the initial steps for angiogenesis, Biotechnol. Prog. 31 (1) (2015) 248–257.

[29] B.E. Sumpio, A.J. Banes, L.G. Levin, G. Johnson Jr., Mechanical stress stimulates aortic endothelial cells to proliferate, J. Vasc. Surg. 6 (3) (1987) 252–256.

[30] X.-m. Liu, D. Ensenat, H. Wang, A.I. Schafer, W. Durante, Physiologic cyclic stretch inhibits apoptosis in vascular endothelium, FEBS (Fed. Eur. Biochem. Soc.) Lett. 541 (1–3) (2003) 52–56.

[31] W. Li, B.E. Sumpio, Strain-induced vascular endothelial cell proliferation requires PI3K-dependent mTOR-4E-BP1 signal pathway, Am. J. Physiol. Heart Circ. Physiol. 288 (4) (2005) H1591–H1597.

[32] B. Kou, J. Zhang, D.R. Singer, Effects of cyclic strain on endothelial cell apoptosis and tubulogenesis are dependent on ROS production via NAD(P)H subunit p22phox, Microvasc. Res. 77 (2) (2009) 125–133.

[33] P. Augat, M. Hollensteiner, C. von Rüden, The role of mechanical stimulation in the enhancement of bone healing, Injury 52 (2021) S78–S83.

[34] K.F. Eichholz, F.E. Freeman, P. Pitacco, J. Nulty, D. Ahern, R. Burdis, D.C. Browe, O. Garcia, D.A. Hoey, D.J. Kelly, Scaffold microarchitecture regulates angiogenesis and the regeneration of large bone defects, Biofabrication 14 (4) (2022) 045013.

[35] M. Paris, A. Götz, I. Hettrich, C.M. Bidan, J.W.C. Dunlop, H. Razi, I. Zizak, D. W. Hutmacher, P. Fratzl, G.N. Duda, W. Wagermaier, A. Cipitria, Scaffold curvature-mediated novel biomineralization process originates a continuous soft tissue-to-bone interface, Acta Biomater. 60 (2017) 64–80.

[36] L. Rodríguez-Montaño Ó, C.J. Cortés-Rodríguez, A.E. Uva, M. Fiorentino, M. Gattullo, G. Monno, A. Boccaccio, Comparison of the mechanobiological performance of bone tissue scaffolds based on different unit cell geometries, J. Mech. Behav. Biomed. Mater. 83 (2018) 28–45.

[37] M. Jaber, P.S.P. Poh, G.N. Duda, S. Checa, PCL strut-like scaffolds appear superior to gyroid in terms of bone regeneration within a long bone large defect: an in silico study, Front. Bioeng. Biotechnol. 10 (2022).

[38] X. Sun, Y. Kang, J. Bao, Y. Zhang, Y. Yang, X. Zhou, Modeling vascularized bone regeneration within a porous biodegradable CaP scaffold loaded with growth factors, Biomaterials 34 (21) (2013) 4971–4981.

[39] A. Artel, H. Mehdizadeh, Y.C. Chiu, E.M. Brey, A. Cinar, An agent-based model for the investigation of neovascularization within porous scaffolds, Tissue Eng. 17 (17–18) (2011) 2133–2141.

[40] H. Mehdizadeh, S. Sumo, E.S. Bayrak, E.M. Brey, A. Cinar, Three-dimensional modeling of angiogenesis in porous biomaterial scaffolds, Biomaterials 34 (12) (2013) 2875–2887.

[41] H. Mehdizadeh, E.S. Bayrak, C. Lu, S.I. Somo, B. Akar, E.M. Brey, A. Cinar, Agent-based modeling of porous scaffold degradation and vascularization: optimal scaffold design based on architecture and degradation dynamics, Acta Biomater. 27 (2015) 167–178.

[42] C. Perier-Metz, A. Cipitria, D.W. Hutmacher, G.N. Duda, S. Checa, An in silico model predicts the impact of scaffold design in large bone defect regeneration, Acta Biomater. 145 (2022) 329–341.

[43] G. Nasello, A. Vautrin, J. Pitocchi, M. Wesseling, J.H. Kuiper, M.Á. Pérez, J. M. García-Aznar, Mechano-driven regeneration predicts response variations in large animal model based on scaffold implantation site and individual mechano-sensitivity, Bone 144 (2021) 115769.

[44] K.F. Eichholz, I. Gonçalves, X. Barceló, A.S. Federici, D.A. Hoey, D.J. Kelly, How to design, develop and build a fully-integrated melt electrowriting 3D printer, Addit. Manuf. 58 (2022) 102998.

[45] F.E. Freeman, P. Pitacco, L.H.A. van Dommelen, J. Nulty, D.C. Browe, J.-Y. Shin, E. Alsberg, D.J. Kelly, 3D bioprinting spatiotemporally defined patterns of growth factors to tightly control tissue regeneration, Sci. Adv. 6 (33) (2020) eabb5093.

[46] J. Nulty, F.E. Freeman, D.C. Browe, R. Burdis, D.P. Ahern, P. Pitacco, Y.B. Lee, E. Alsberg, D.J. Kelly, 3D bioprinting of prevascularised implants for the repair of critically-sized bone defects, Acta Biomater. 126 (2021) 154–169.

[47] K.F. Eichholz, S. Von Euw, R. Burdis, D.J. Kelly, D.A. Hoey, Development of a new bone-mimetic surface treatment platform: nanoneedle hydroxyapatite (nnHA) coating, Adv. Healthcare Mater. 9 (24) (2020) 2001102.

[48] C.A. Dessalles, C. Leclech, A. Castagnino, A.I. Barakat, Integration of substrate- and flow-derived stresses in endothelial cell mechanobiology, Commun. Biol. 4 (1) (2021) 764.

[49] E. Borgiani, G.N. Duda, B.M. Willie, S. Checa, Bone morphogenetic protein 2-induced cellular chemotaxis drives tissue patterning during critical-sized bone defect healing: an in silico study, Biomech. Model. Mechanobiol. 20 (4) (2021) 1627–1644.

[50] C. Schwarz, D. Wulsten, A. Ellinghaus, J. Lienau, B.M. Willie, G.N. Duda, Mechanical load modulates the stimulatory effect of BMP2 in a rat nonunion model, Tissue Eng. 19 (1–2) (2013) 247–254.

[51] T. Wehner, U. Wolfram, T. Henzler, F. Niemeyer, L. Claes, U. Simon, Internal forces and moments in the femur of the rat during gait, J. Biomech. 43 (13) (2010) 2473–2479.

[52] S. Checa, P.J. Prendergast, G.N. Duda, Inter-species investigation of the mechano-regulation of bone healing: comparison of secondary bone healing in sheep and rat, J. Biomech. 44 (7) (2011) 1237–1245.

[53] C.G. Pitt, F.I. Chasalow, Y.M. Hibionada, D.M. Klimas, A. Schindler, Aliphatic polyesters. I. The degradation of poly(ε-caprolactone) in vivo, J. Appl. Polym. Sci. 26 (11) (1981) 3779–3787.

[54] R.H. Wehrenberg, Lactic Acid Polymers: Strong, Degradable Thermoplastics, vol. 94, 1981, p. 3.

[55] I. Engelberg, J. Kohn, Physico-mechanical properties of degradable polymers used in medical applications: a comparative study, Biomaterials 12 (3) (1991) 292–304.

[56] T.F. Vandamme, R. Legras, Physico-mechanical properties of poly(ε-caprolactone) for the construction of rumino-reticulum devices for grazing animals, Biomaterials 16 (18) (1995) 1395–1400.

[57] D.S. Rosa, I.C. Neto, M.R. Calil, A.G. Pedroso, C.P. Fonseca, S. Neves, Evaluation of the thermal and mechanical properties of poly(ε-caprolactone), low-density polyethylene, and their blends, J. Appl. Polym. Sci. 91 (6) (2004) 3909–3914.

[58] V.M. Correlo, L.F. Boesel, M. Bhattacharya, J.F. Mano, N.M. Neves, R.L. Reis, Hydroxyapatite reinforced chitosan and polyester blends for biomedical applications, Macromol. Mater. Eng. 290 (12) (2005) 1157–1165.

[59] S. Eshraghi, S. Das, Mechanical and microstructural properties of polycaprolactone scaffolds with one-dimensional, two-dimensional, and three-dimensional orthogonally oriented porous architectures produced by selective laser sintering, Acta Biomater. 6 (7) (2010) 2467–2476.

[60] H. Isaksson, C.C. van Donkelaar, R. Huiskes, K. Ito, A mechano-regulatory bone-healing model incorporating cell-phenotype specific activity, J. Theor. Biol. 252 (2) (2008) 230–246.

[61] J. Mehl, S.K. Farahani, E. Brauer, A. Klaus-Bergmann, T. Thiele, A. Ellinghaus, E. Bartels-Klein, K. Koch, K. Schmidt-Bleek, A. Petersen, H. Gerhardt, V. Vogel, G. N. Duda, External mechanical stability regulates hematoma vascularization in bone healing rather than endothelial YAP/TAZ mechanotransduction, Adv. Sci. 11 (13) (2024) 2307050.

[62] A. Cipitria, C. Lange, H. Schell, W. Wagermaier, J.C. Reichert, D.W. Hutmacher, P. Fratzl, G.N. Duda, Porous scaffold architecture guides tissue formation, J. Bone Miner. Res. 27 (6) (2012) 1275–1288.

[63] M. Werner, N.A. Kurniawan, G. Korus, C.V.C. Bouten, A. Petersen, Mesoscale substrate curvature overrules nanoscale contact guidance to direct bone marrow stromal cell migration, J. R. Soc. Interface 15 (145) (2018) 20180162.

[64] C. Perier-Metz, G.N. Duda, S. Checa, Mechano-biological computer model of scaffold-supported bone regeneration: effect of bone graft and scaffold structure on large bone defect tissue patterning, Front. Bioeng. Biotechnol. 8 (2020) 585799.

[65] C. Dazzi, J. Mehl, M. Benamar, H. Gerhardt, P. Knaus, G.N. Duda, S. Checa, External mechanical loading overrules cell-cell mechanical communication in sprouting angiogenesis during early bone regeneration, PLoS Comput. Biol. 19 (11) (2023) e1011647.

[66] F. Rossi, H.E. MacLean, W. Yuan, R.O. Francis, E. Semenova, C.S. Lin, H. M. Kronenberg, D. Cobrinik, p107 and p130 coordinately regulate proliferation, Cbfa1 expression, and hypertrophic differentiation during endochondral bone development, Dev. Biol. 247 (2) (2002) 271–285.

[67] C.l. Colnot, Z. Thompson, T. Miclau, Z. Werb, J.A. Helms, Altered fracture repair in the absence of MMP9, Development 130 (17) (2003) 4123–4133.

[68] H.-P. Gerber, T.H. Vu, A.M. Ryan, J. Kowalski, Z. Werb, N. Ferrara, VEGF couples hypertrophic cartilage remodeling, ossification and angiogenesis during endochondral bone formation, Nat. Med. 5 (6) (1999) 623–628.

[69] P.C. Dartsch, E. Betz, Response of cultured endothelial cells to mechanical stimulation, Basic Res. Cardiol. 84 (3) (1989) 268–281.

[70] J. Kleinheinz, U. Stratmann, U. Joos, H.-P. Wiesmann, VEGF-activated angiogenesis during bone regeneration, J. Oral Maxillofac. Surg. 63 (9) (2005) 1310–1316.

[71] M.A. Ruehle, E.A. Eastburn, S.A. LaBelle, L. Krishnan, J.A. Weiss, J.D. Boerckel, L. B. Wood, R.E. Guldberg, N.J. Willett, Extracellular matrix compression temporally regulates microvascular angiogenesis, Sci. Adv. 6 (34) (2020).

[72] P. Carmeliet, Angiogenesis in health and disease, Nat. Med. 9 (6) (2003) 653–660.

[73] S. Checa, P.J. Prendergast, A mechanobiological model for tissue differentiation that includes angiogenesis: a lattice-based modeling approach, Ann. Biomed. Eng. 37 (1) (2009) 129–145.

[74] P.A. Appeddu, B.D. Shur, Molecular analysis of cell surface beta-1,4-galactosyltransferase function during cell migration, Proc. Natl. Acad. Sci. 91 (6) (1994) 2095–2099.

[75] B.M. Kenyon, E.E. Voest, C.C. Chen, E. Flynn, J. Folkman, R.J. D'Amato, A model of angiogenesis in the mouse cornea, Investig. Ophthalmol. Vis. Sci. 37 (8) (1996) 1625–1632.

[76] M. Abramoff, P. Magalhães, S.J. Ram, Image processing with ImageJ, Biophot. Int. 11 (2003) 36–42.

[77] B. Schmid, J. Schindelin, A. Cardona, M. Longair, M. Heisenberg, A high-level 3D visualization API for java and ImageJ, BMC Bioinf. 11 (1) (2010) 274.

[78] P.J. Prendergast, R. Huiskes, K. Søballe, Biophysical stimuli on cells during tissue differentiation at implant interfaces, J. Biomech. 30 (6) (1997) 539–548.

[79] S. Van Bael, Y.C. Chai, S. Truscello, M. Moesen, G. Kerckhofs, H. Van Oosterwyck, J.P. Kruth, J. Schrooten, The effect of pore geometry on the in vitro biological behavior of human periosteum-derived cells seeded on selective laser-melted Ti6Al4V bone scaffolds, Acta Biomater. 8 (7) (2012) 2824–2834.

[80] M. Bohner, R.J. Miron, A proposed mechanism for material-induced heterotopic ossification, Mater. Today 22 (2019) 132–141.

[81] H. Wang, W. Zhi, X. Lu, X. Li, K. Duan, R. Duan, Y. Mu, J. Weng, Comparative studies on ectopic bone formation in porous hydroxyapatite scaffolds with complementary pore structures, Acta Biomater. 9 (9) (2013) 8413–8421.

[82] J.D. Boerckel, B.A. Uhrig, N.J. Willett, N. Huebsch, R.E. Guldberg, Mechanical regulation of vascular growth and tissue regeneration in vivo, Proc. Natl. Acad. Sci. U. S. A. 108 (37) (2011) E674–E680.

[83] L.C. Gerstenfeld, D.M. Cullinane, G.L. Barnes, D.T. Graves, T.A. Einhorn, Fracture healing as a post-natal developmental process: molecular, spatial, and temporal aspects of its regulation, J. Cell. Biochem. 88 (5) (2003) 873–884.

[84] M.N. Nakatsu, R.C.A. Sainson, S. Pérez-del-Pulgar, J.N. Aoto, M. Aitkenhead, K. L. Taylor, P.M. Carpenter, C.C.W. Hughes, VEGF121 and VEGF165 regulate blood vessel diameter through vascular endothelial growth factor receptor 2 in an in vitro angiogenesis model, Lab. Invest. 83 (12) (2003) 1873–1885.

[85] N. Baeyens, S. Nicoli, B.G. Coon, T.D. Ross, K. Van den Dries, J. Han, H. M. Lauridsen, C.O. Mejean, A. Eichmann, J.-L. Thomas, J.D. Humphrey, M. A. Schwartz, Vascular remodeling is governed by a VEGFR3-dependent fluid shear stress set point, eLife 4 (2015) e04645.

[86] B.N. Brown, B.M. Sicari, S.F. Badylak, Rethinking regenerative medicine: a macrophage-centered approach, Front. Immunol. 5 (2014), 2014.

[87] D. Abebayehu, A.J. Spence, M.J. McClure, T.T. Haque, K.O. Rivera, J.J. Ryan, Polymer scaffold architecture is a key determinant in mast cell inflammatory and angiogenic responses, J. Biomed. Mater. Res. 107 (4) (2019) 884–892.

[88] E. Saino, M.L. Focarete, C. Gualandi, E. Emanuele, A.I. Cornaglia, M. Imbriani, L. Visai, Effect of electrospun fiber diameter and alignment on macrophage activation and secretion of proinflammatory cytokines and chemokines, Biomacromolecules 12 (5) (2011) 1900–1911.

[89] P.M. Mountziaris, A.G. Mikos, Modulation of the inflammatory response for enhanced bone tissue regeneration, Tissue Eng., Part B 14 (2) (2008) 179–186.

[90] Y. Wang, T. Azaïs, M. Robin, A. Vallée, C. Catania, P. Legriel, G. Pehau-Arnaudet, F. Babonneau, M.-M. Giraud-Guille, N. Nassif, The predominant role of collagen in the nucleation, growth, structure and orientation of bone apatite, Nat. Mater. 11 (8) (2012) 724–733.

[91] C.D. Davidson, W.Y. Wang, I. Zaimi, D.K.P. Jayco, B.M. Baker, Cell force-mediated matrix reorganization underlies multicellular network assembly, Sci. Rep. 9 (1) (2019) 12.

[92] J. Jin, R.T. Jaspers, G. Wu, J.A.M. Korfage, J. Klein-Nulend, A.D. Bakker, Shear stress modulates osteoblast cell and nucleus morphology and volume, Int. J. Mol. Sci. 21 (21) (2020) 8361.

[93] A. Matsugaki, N. Fujiwara, T. Nakano, Continuous cyclic stretch induces osteoblast alignment and formation of anisotropic collagen Fiber matrix, Acta Biomater. 9 (7) (2013) 7227–7235.

[94] C. Korn, Hellmut G. Augustin, Mechanisms of vessel pruning and regression, Dev. Cell 34 (1) (2015) 5–17.